Computational implementation of a non-linear kinematic hardening formulation for tension–torsion multiaxial fatigue calculations

CrossMark

Hao Wu [a], Marco Antonio Meggiolaro [b,*], Jaime Tupiassú Pinho de Castro [b]

[a] School of Aerospace Engineering and Applied Mechanics, Tongji University, 1239 Siping Road, Shanghai, PR China
[b] Department of Mechanical Engineering, Pontifical Catholic University of Rio de Janeiro, Rua Marquês de São Vicente 225 – Gávea, Rio de Janeiro, RJ 22451-900, Brazil

A B S T R A C T

The calculation of elastoplastic strains from stress histories, or vice-versa, is an important computational step in low-cycle fatigue analyses. This step is a challenging task for general multiaxial non-proportional (NP) loading histories, where the principal stress directions are not constant, requiring 6D incremental plasticity calculations to correlate the six stress with the six strain components considering plasticity effects. However, a large number of multiaxial fatigue problems only involve combined tension and/or bending and torsion loads, which are associated with only one normal and one shear stress component. The use of a special 2D formulation, instead of 6D, can greatly simplify the necessary incremental plasticity calculations for these practical problems. In this work, a new 2D tension–torsion incremental plasticity formulation is introduced, integrating non-linear kinematic (NLK) hardening models and NP hardening effects in a very efficient way, exactly reproducing tension–torsion calculations from more general 6D models, but with less than one fifth of the computational cost. The proposed 2D approach is validated by comparing NP strain-controlled tension–torsion experiments in 316L steel tubular specimens, a material that presents significant NP hardening effects, with experimental and predicted stress paths, calculated either with 6D or the proposed 2D formulation.

© 2016 Elsevier Ltd. All rights reserved.

1. Introduction

Most engineering applications involve either known stress or strain histories, but not both. New components are normally designed based on stress histories calculated or estimated from measured or specified design loads, whereas advanced structural integrity evaluations use strain histories properly measured in the field under actual service conditions; since stresses cannot be measured, they can only be calculated. However, most multiaxial fatigue models require both the stress and the strain histories to quantify the damage induced by the loading history.

Calculation of multiaxial stresses from given strains or vice-versa is a trivial task if the load at the critical point is linear elastic (LE), only requiring the application of Hooke's law. But for low-cycle fatigue calculations, where cyclic plasticity effects can be very significant, incremental plasticity models are usually needed to correlate multiaxial stresses and strains, especially under variable amplitude (VA) non-proportional (NP) loadings. Two approaches can be followed in these cases to estimate crack

initiation lives: performing global elastoplastic (EP) incremental finite element (FE) calculations for the entire component along the loading history, a computationally prohibitive task for VA load histories with many cycles or events; or instead use a much simpler global–local approach [1–5], where a single LE FE calculation on the entire piece is performed for a static unit value of each applied loading, followed by local incremental plasticity calculations at every load step only at the critical point(s), to correct for plasticity effects.

The former approach requires global Finite Element (FE) calculations to evaluate the interaction among EP stresses and strains, considering as well stress gradient effects near the critical point. This global EP FE approach thus needs to adopt an incremental plasticity formulation in every element of the mesh that represents the studied structural component that suffers plastic strains. This requirement is computationally very intensive, especially when dealing with long loading histories, since it implies in having to solve the EP FE problem for the entire piece for every load increment of every load cycle (or of every load event in complex VA cases, where cycles cannot be identified).

The global–local approach, on the other hand, can be very accurate and computationally much more efficient if carefully performed, as described next. Consider a general case of N applied

* Corresponding author. Tel.: +55 21 3527 1424; fax: +55 21 3527 1165.
  E-mail addresses: wuhao@tongji.edu.cn (H. Wu), meggi@puc-rio.br (M.A. Meggiolaro), jtcastro@puc-rio.br (J.T.P. de Castro).

loads (which could be e.g. forces, moments, or displacements), with time histories given by $F_1(t), F_2(t), \ldots$, see Fig. 1. A constant unit load $F_1(t) = 1$ is imposed to the piece in a LE FE calculation, to obtain the resulting six stress and strain components at the critical point, which would constitute the LE stress and strain influence factors $K_{\sigma x1}, K_{\sigma y1}, K_{\sigma z1}, K_{\sigma xy1}, K_{\sigma xz1}, K_{\sigma yz1}, K_{\varepsilon x1}, K_{\varepsilon y1}, K_{\varepsilon z1},$ $K_{\varepsilon xy1}, K_{\varepsilon xz1},$ and $K_{\varepsilon yz1}$, see Fig. 1. Another LE FE calculation with only $F_2(t) = 1$ would then obtain the associated stress and strain influence factors $K_{\sigma x2}, K_{\sigma y2}, \ldots, K_{\varepsilon yz2}$, and so on. These factors can then be organized into LE stress and strain influence matrices, as shown in Fig. 1, which calculate the so-called pseudo-stresses and pseudo-strains (represented with a tilde "~" mark, see Fig. 1), i.e. stresses and strains assumed to be LE, even though they in general might not be elastic and thus later require elastoplastic corrections.

These matrices are then used to compute the so-called pseudo-stresses and pseudo-strains which, as mentioned above, are fictitious quantities calculated assuming the material follows Hooke's law at the critical point of the piece. The pseudo-stresses $\tilde{\vec{\sigma}}$ and strains $\tilde{\vec{\varepsilon}}$ are obtained after multiplying the actual value of the loadings $F_1(t), F_2(t), \ldots$, at each instant t by their associated LE influence factors, and adding them at the critical point using the superposition principle.

If the critical point is not evident, then these matrices need to be calibrated for each potential critical location. The potential location that results in the highest accumulated multiaxial fatigue damage is then the critical point where the crack is expected to initiate. The direction of such a crack could also be calculated using the critical-plane approach for all candidate planes at this critical point [6].

The resulting pseudo-histories $\tilde{\vec{\sigma}}(t)$ and $\tilde{\vec{\varepsilon}}(t)$ can deal with multiple in- or out-of-phase loading sources applied to the structural component, but they are LE values that in general still require EP corrections to reproduce the true stresses and strains at its critical point. Indeed, in their LE form they can only be used in the absence of significant macroscopic plasticity at the critical point, i.e. they are only useful for high-cycle fatigue calculations that do not involve residual stresses induced by eventual overloads. Otherwise, a proper multiaxial incremental plasticity formulation must be used to account for cyclic kinematic, isotropic, and NP hardening effects in the EP stress/strain behavior, in general considering notch stress and strain concentration effects [1–5]. However, the involved calculations require the solution of a set of dozens of stiff differential equations, a challenging task that prevents its widespread use in engineering problems without the aid of advanced and dedicated commercial fatigue software, thus involving costs that are usually prohibitive for small companies.

In the following sections, a new simplified yet accurate incremental plasticity formulation is fully developed for combined tension–torsion problems, a very important practical case induced by normal and/or bending and torsional loads in common components such as shafts and beams. It is shown that the full 6D stress–strain problem does not need to be solved in such cases, which can be managed using a 2D reduced-order formulation that much simplifies its computer implementation and also reduces the calculation time in more than 80%.

2. Tension–torsion hardening formulation

Tension–torsion incremental plasticity calculations are most efficiently performed in a 2D stress space $\sigma_x \times \tau_{xy}\sqrt{3}$, where σ_x is the normal and $\tau_{xy}\sqrt{3}$ is the effective shear stress. The yield surface is defined as the root locus of the stress states $\vec{s} = \begin{bmatrix} \sigma_x & \tau_{xy}\sqrt{3} \end{bmatrix}^T$ (or stress points, where T stands for transpose of a vector or matrix) where the material starts to yield. Under tension–torsion, the yield surface can be described as a circle in this diagram if the material follows the von Mises criterion, since

$$\vec{s} = \begin{bmatrix} \sigma_x & \tau_{xy}\sqrt{3} \end{bmatrix}^T \Rightarrow Y = |\vec{s}|^2 - S^2 = \left(\sigma_x^2 + 3\tau_{xy}^2 \right) - S^2 = 0 \qquad (1)$$

where S is the current radius of the yield surface, e.g. the monotonic yield strength S_Y for a tensile test or the cyclic yield strength S_{Yc} for a cyclically-stabilized loading, and $Y = 0$ is the yield function.

2.1. Kinematic hardening formulation

Loading a piece above its yield limit in one direction reduces (in absolute value) its yield strength in the opposite direction, a phenomenon known as the Bauschinger effect. For a tension–torsion history, this effect can be represented as a translation of the yield surface, whose center translates to a so-called backstress position $\vec{\beta} = \begin{bmatrix} \beta_x & \beta_{xy}\sqrt{3} \end{bmatrix}^T$, see Fig. 2 [7]. This backstress vector is the quantity that stores the plastic memory effects required for kinematic hardening calculations.

Assuming the normal stresses in the x direction, if the material is isotropic and thus has symmetry in the y and z directions, then its elastic (el) and plastic (pl) strain components can also be represented in 2D, by

$$\vec{e}_{el} \equiv (1 + \nu) \cdot \begin{bmatrix} \varepsilon_{x_{el}} & \frac{\gamma_{xy_{el}}}{2 \cdot (1+\nu)}\sqrt{3} \end{bmatrix}^T \text{ and } \vec{e}_{pl} \equiv \frac{3}{2} \cdot \begin{bmatrix} \varepsilon_{x_{pl}} & \frac{\gamma_{xy_{pl}}}{\sqrt{3}} \end{bmatrix}^T \qquad (2)$$

where ν is Poisson's ratio, ε stands for normal and γ for shear strains.

This efficient representation is a 2D strain sub-space from the 5D deviatoric space introduced in [8] and further detailed in [9].
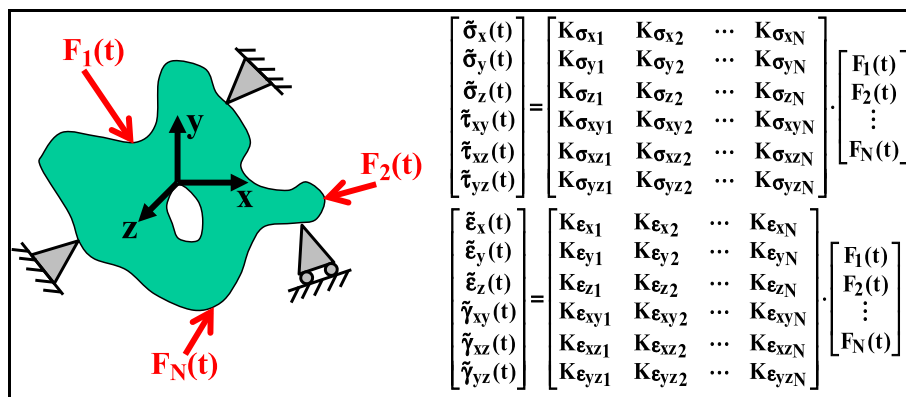

$$\begin{bmatrix} \tilde{\sigma}_x(t) \\ \tilde{\sigma}_y(t) \\ \tilde{\sigma}_z(t) \\ \tilde{\tau}_{xy}(t) \\ \tilde{\tau}_{xz}(t) \\ \tilde{\tau}_{yz}(t) \end{bmatrix} = \begin{bmatrix} K_{\sigma x1} & K_{\sigma x2} & \cdots & K_{\sigma xN} \\ K_{\sigma y1} & K_{\sigma y2} & \cdots & K_{\sigma yN} \\ K_{\sigma z1} & K_{\sigma z2} & \cdots & K_{\sigma zN} \\ K_{\sigma xy1} & K_{\sigma xy2} & \cdots & K_{\sigma xyN} \\ K_{\sigma xz1} & K_{\sigma xz2} & \cdots & K_{\sigma xzN} \\ K_{\sigma yz1} & K_{\sigma yz2} & \cdots & K_{\sigma yzN} \end{bmatrix} \cdot \begin{bmatrix} F_1(t) \\ F_2(t) \\ \vdots \\ F_N(t) \end{bmatrix}$$

$$\begin{bmatrix} \tilde{\varepsilon}_x(t) \\ \tilde{\varepsilon}_y(t) \\ \tilde{\varepsilon}_z(t) \\ \tilde{\gamma}_{xy}(t) \\ \tilde{\gamma}_{xz}(t) \\ \tilde{\gamma}_{yz}(t) \end{bmatrix} = \begin{bmatrix} K_{\varepsilon x1} & K_{\varepsilon x2} & \cdots & K_{\varepsilon xN} \\ K_{\varepsilon y1} & K_{\varepsilon y2} & \cdots & K_{\varepsilon yN} \\ K_{\varepsilon z1} & K_{\varepsilon z2} & \cdots & K_{\varepsilon zN} \\ K_{\varepsilon xy1} & K_{\varepsilon xy2} & \cdots & K_{\varepsilon xyN} \\ K_{\varepsilon xz1} & K_{\varepsilon xz2} & \cdots & K_{\varepsilon xzN} \\ K_{\varepsilon yz1} & K_{\varepsilon yz2} & \cdots & K_{\varepsilon yzN} \end{bmatrix} \cdot \begin{bmatrix} F_1(t) \\ F_2(t) \\ \vdots \\ F_N(t) \end{bmatrix}$$

Fig. 1. FE-calibrated linear elastic matrices correlating several applied scalar load histories with the twelve resulting pseudo-stress and pseudo-strain histories at the critical point.
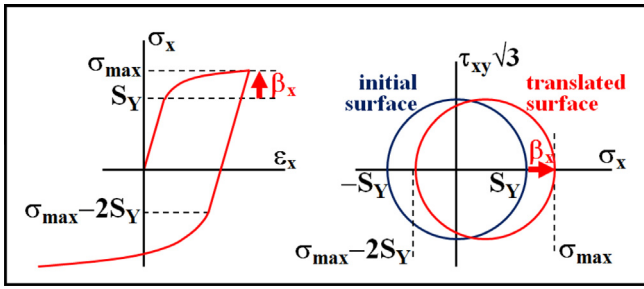
Fig. 2. Kinematic hardening in the x direction and the associated yield surface translation in the $\sigma_x \times \tau_{xy}\sqrt{3}$ von Mises diagram.

This definition of the 2D elastic strain simplifies Hooke's law to a much more convenient scalar relation:

$$\vec{e}_{el} \equiv \left[(1+v) \cdot \varepsilon_{x_{el}} \quad \frac{\gamma_{xy_{el}}}{2}\sqrt{3} \right]^T = \left[\frac{\sigma_x}{E/(1+v)} \quad \frac{\tau_{xy}}{2G}\sqrt{3} \right]^T$$
$$= \frac{\vec{s}}{2G} \quad \Rightarrow \quad \vec{e}_{el} = \frac{\vec{s}}{2G} \tag{3}$$

where E is Young's modulus and $G \equiv E/(2+2v)$ is the shear modulus. The 2D plastic strain $\vec{e}_{pl}$ can then be obtained from the 2D $\vec{e}_{el}$ by replacing the elastic Poisson ratio v with 0.5. Another advantage of these 2D strain spaces is that their norm is proportional to the elastic and plastic parts of the associated von Mises strain.

Note however that, in notch tips or in complex geometries with different transversal constraint factors in the y and z directions, it is possible to have $\varepsilon_y \neq \varepsilon_z$ or non-zero $\sigma_y \neq \sigma_z$ under plane-strain states even for isotropic materials. Such problems require instead an incremental plasticity formulation with higher dimension to describe their multiaxial $\sigma\varepsilon$ behavior. Despite this limitation, the 2D formulation presented in this work is perfectly suitable for simulating the behavior e.g. of tubular tension–torsion test specimens, the most adopted geometry for evaluating multiaxial properties of materials [7], providing a valuable tool to simulate and analyze the behavior of materials with a much lower computational cost than higher dimension models.

Infinitesimal plastic strain increments $d\vec{e}_{pl}$ can be correlated with infinitesimal stress increments $d\vec{s}$ using the Prandtl–Reuss rule

$$d\vec{e}_{pl} = \frac{1}{P} \cdot (d\vec{s}^T \cdot \vec{n}) \cdot \vec{n} \tag{4}$$

where P is the current generalized plastic modulus, and $\vec{n}$ is the normal unit vector perpendicular to the yield surface $Y = 0$ at the current stress state, calculated from

$$\vec{n} = (\vec{s} - \vec{\beta})/S, \text{ if } |\vec{s} - \vec{\beta}| = S \tag{5}$$

Clearly, if the current stress state is elastic, then it is inside the yield surface, thus $|\vec{s} - \vec{\beta}| < S$ and the normal unit vector (which is only used during plastic straining) is not defined.

The two main attributes of a kinematic hardening model are to compute the evolution of the center of the yield surface, i.e. the evolution of the backstress $\vec{\beta}$, and to compute the current value of the plastic modulus P. There are several models to calculate the current value of P and of the infinitesimal yield surface translation $d\vec{\beta}$ during plastic straining, which can be divided into three main classes: Mróz-multi-surface [10,11], two-surface [12,13], and non-linear [14] kinematic hardening models. Mróz-multi-surface models result in a multi-linear description of the stress–strain curve, where P is assumed as piecewise constant; this linearity prevents such models to correctly predict complex (although not unusual) plasticity effects such as ratcheting and

mean stress relaxation, which can be very important in practical applications [15]. Non-linear kinematic (NLK) hardening models solve this issue, adopting non-linear equations to describe the evolution of P, therefore their (more general) formulation is the one adopted in this work. Two-surface models combine elements of both NLK and Mróz-multi-surface kinematic hardening models, however their description of plastic memory is limited and not recommended for complex variable amplitude (VA) histories commonly found in fatigue.

The original NLK model, proposed by Armstrong and Frederick [16], uses non-linear equations to calculate the incremental translation $d\vec{\beta}$ of the yield surface at every load step, however its plastic memory capabilities are too limited to be applied to more complex VA loading. Chaboche [17] improved their model, indirectly introducing some multi-surface elements into the NLK models, using a better non-linear formulation instead of the simplistic Mróz-multi-linear approach. Chaboche assumed that the yield surface center $\vec{\beta}$ at every load step can be represented as a sum of M backstress components $\vec{\beta}_i$ ($i = 1, 2, \ldots, M$), see Fig. 3, thus

$$\vec{\beta} \equiv \vec{\beta}_1 + \vec{\beta}_2 + \cdots + \vec{\beta}_M \tag{6}$$

Each backstress component $\vec{\beta}_i$ is associated with a saturation value Δr_i that limits the maximum value of its norm, thus $|\vec{\beta}_i| \leqslant \Delta r_i$. A zero norm is related to an unhardened material state with high generalized plastic modulus P (indeed, note that a purely elastic state would have $P \to \infty$), while a saturated norm $|\vec{\beta}_i| = \Delta r_i$ represents a hardened state with much lower P (conversely, a plastic collapse condition with $\vec{e}_{pl} \to \infty$ would have $P \to 0$). Moreover, each $\vec{\beta}_i$ is also associated with a generalized plastic modulus coefficient p_i, used in the calculation of the current value of P through

$$P = (2/3) \cdot (p_1 \cdot \vec{v}_1^T + p_2 \cdot \vec{v}_2^T + \cdots + p_M \cdot \vec{v}_M^T) \cdot \vec{n} \tag{7}$$

where $\vec{n}$ has been defined in Eq. (5) and $\vec{v}_i$ are translation direction vectors for each surface that depend on the adopted NLK model.

Eq. (7) satisfies the consistency condition, which prevents the current stress state $\vec{s}$ from moving outside the yield surface (i.e. prevents the impossible configuration $|\vec{s} - \vec{\beta}| > S$), as long as the infinitesimal translations $d\vec{\beta}_i$ of the backstress components $\vec{\beta}_i$ are such that

$$d\vec{\beta}_i = \begin{cases} p_i \cdot \vec{v}_i \cdot dp, & \text{if } |\vec{\beta}_i| < \Delta r_i \text{ (unsaturated condition for } \vec{\beta}_i) \\ 0, & \text{if } |\vec{\beta}_i| = \Delta r_i \text{ (saturated condition for } \vec{\beta}_i) \end{cases}, i = 1, 2, \ldots, M \tag{8}$$

where $dp \equiv (2/3) \cdot |d\vec{e}_{pl}|$ is the equivalent plastic strain increment, which from Eq. (4) results in
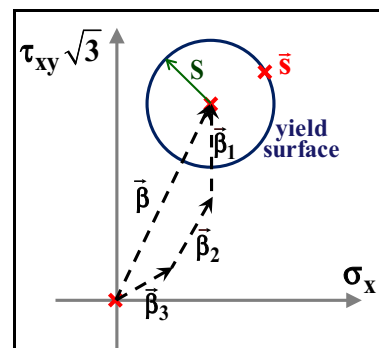

Fig. 3. Representation of the yield surface center in the $\sigma_x \times \tau_{xy}\sqrt{3}$ von Mises diagram using $M = 3$ backstress components.

$$dp = (2/3) \cdot (d\vec{s}^T \cdot \vec{n})/P \qquad (9)$$

Using the above notation, the only difference among the main NLK models is the choice of the equation for the translation direction vectors $\vec{v}_i$. A generalized surface translation rule has been proposed in a companion work [18]:

$$\vec{v}_i = \underbrace{\vec{n} \cdot \Delta r_i}_{\substack{Prager-\\Ziegler}} - \chi_i^* \cdot m_i^* \cdot \gamma_i \cdot \left[\underbrace{\delta_i \cdot \vec{\beta}_i}_{\substack{dynamic\\recovery}} + \underbrace{(1 - \delta_i) \cdot \left(\vec{\beta}_i^T \cdot \vec{n}\right) \cdot \vec{n}}_{\substack{radial\\return}} \right] \qquad (10)$$

where the scalar functions χ_i^* and m_i^* are defined as

$$\chi_{i*} \equiv \left(\frac{|\vec{\beta}_i|}{\Delta r_i} \right)^{\chi_i} \text{ and } m_{i*} \equiv \begin{cases} \left[\vec{\beta}_i^T \cdot \vec{n} / |\vec{\beta}_i| \right]^{m_i}, \text{ if } \vec{\beta}_i^T \cdot \vec{n} > 0 \\ 0, \text{ if } \vec{\beta}_i^T \cdot \vec{n} \leqslant 0 \text{ and } m_i \neq 0 \\ \quad (\text{or } 1 \text{ if } m_i = 0) \end{cases} \qquad (11)$$

where χ_i, m_i, γ_i, and δ_i are adjustable ratcheting parameters for each backstress component.

These versatile equations can reproduce Chaboche's model [17] if $\chi_i = \gamma_i = \delta_i = 1$ and $m_i = 0$; Jiang–Sehitoglu's model [19,20] for $\gamma_i = \delta_i = 1, m_i = 0$ and adjustable $0 < \chi_i < \infty$; Ohno–Wang II [21] for $\gamma_i = \delta_i = m_i = 1$ and adjustable $0 < \chi_i < \infty$; Delobelle's [22] for $\chi_i = m_i = 0$ and adjustable $0 < \gamma_i < 1$ and $0 < \delta_i < 1$; Burlet–Cailletaud's model [23] for $\chi_i = \delta_i = m_i = 0$ and adjustable $0 < \gamma_i < 1$; among others.

Replacing Eq. (10) into Eq. (7), the generalized plastic modulus becomes

$$\begin{aligned} P &= (2/3) \cdot \sum_{i=1}^{M} p_i \cdot \vec{v}_i^T \cdot \vec{n} \\ &= (2/3) \cdot \sum_{i=1}^{M} p_i \cdot \left(\Delta r_i - \chi_i^* \cdot m_i^* \cdot \gamma_i \cdot \vec{\beta}_i^T \cdot \vec{n} \right) \end{aligned} \qquad (12)$$

2.2. Isotropic and NP hardening formulation

Besides kinematic hardening, materials can suffer isotropic and NP hardening effects [18]. Isotropic hardening (or softening) accounts for the changes in the material yield strength associated with the expansion (or the contraction) of the yield surface under cyclic loading, while it gradually changes from the monotonic radius $S = S_Y$ to the cyclic radius $S = S_{Yc}$. Non-proportional (NP) hardening accounts for the increase in the material yield strength associated with the *expansion* of the yield surface caused by NP multiaxial loading histories in sensitive materials like austenitic stainless steels, increasing its radius towards a target value $S_{Yc} \cdot (1\alpha_{NP} \cdot F_{NP})$, where $0 \leqslant F_{NP} \leqslant 1$ is a load-path-dependent *NP hardening factor*, while $0 \leqslant \alpha_{NP} \leqslant 1$ is the material-dependent *additional hardening coefficient*.

In this work, instead of changing the yield surface radius, isotropic and NP hardening effects are accounted for by gradually changing the generalized plastic modulus coefficients p_i, while keeping constant the yield surface radius and all saturation values Δr_i. This approach is much simpler to implement in a computer code, because a varying yield surface radius would result in a more complex consistency condition. Moreover, this approach results in essentially the same stress–strain predictions as the ones with varying radius, as long as the yield surface is defined for a low plastic strain level.

Moreover, since in the NLK formulations the material behavior inside the yield surface is assumed linear elastic, in their implementations it is recommended to adopt a much smaller yield surface than the one associated with the traditional monotonic or cyclic yield strengths arbitrarily defined at a 0.2% plastic strain level, using a value like 0.02% or even 0.002% for the plastic strain threshold to avoid a discontinuous derivative in the calculated stress–strain hysteresis loops. Such smaller yield surfaces can be regarded as a practical elastic limit for the material. Fig. 4 shows measured and simulated stress–strain curves for 316L. The use of a 0.002% threshold allows for a very good calibration of the material stress–strain behavior. On the other hand, incremental plasticity simulations with the yield surface defined for 0.1% or 0.2% levels forces a purely elastic behavior even beyond 370 MPa, making it impossible to accurately describe the stress–strain curve for stresses close to the yield strength. In cyclic plasticity simulations, such a detaching from the actual stress–strain curve can accumulate significant numeric errors.

In the formulation proposed in this work, to account for isotropic and NP hardening, the generalized plastic modulus coefficients $p_i(p)$ evolve from their initial values $p_i(0)$ (from a virgin material) through the equation

$$p_i(p) = p_i(0) \cdot \left\{ \underbrace{[1 + \alpha_{NP} \cdot F_{NP}(p)]}_{NP \ evolution} + \underbrace{(S_Y/S_{Yc} - 1) \cdot e^{-hr_c \cdot p}}_{isotropic \ evolution} \right\}^{1/h_c} \qquad (13)$$

where $p \equiv \int dp$ is the accumulated plastic strain, hr_c is an isotropic hardening rate (typically between 0.5 and 50 for metals), h_c is Ramberg–Osgood's exponent, and the scalar function $F_{NP}(p)$ is the transient value of the load-path-dependent NP factor at every load step.

To compute Eq. (13) for tension–torsion histories, the evolution of $F_{NP}(p)$ is calculated using a 2D version of Tanaka's NP hardening model [24], adopting a symmetric 2×2 (instead of the usual 5×5) polarization tensor $[P_T]$, initially equal to zero and with an evolution equation dictated by the tensor hardening rate hr_T through

$$[dP_T] = (\vec{n} \cdot \vec{n}^T - [P_T]) \cdot hr_T \cdot dp, \text{ where } [P_T] \equiv \begin{bmatrix} P_\sigma & P_{\sigma\tau} \\ P_{\sigma\tau} & P_\tau \end{bmatrix} \qquad (14)$$

If the current plastic straining direction is defined as $\vec{n} \equiv [\begin{array}{cc} n_\sigma & n_\tau \end{array}]^T$, then the scalar evolution equations for the elements from $[P_T]$ can be written as

$$dP_\sigma = (n_\sigma^2 - P_\sigma) \cdot hr_T \cdot dp, \quad dP_\tau = (n_\tau^2 - P_\tau) \cdot hr_T \cdot dp \text{ and}$$
$$dP_{\sigma\tau} = (n_\sigma n_\tau - P_{\sigma\tau}) \cdot hr_T \cdot dp \qquad (15)$$

Then, from the above 2D formulation, it is possible to show that Tanaka's NP hardening model results in an evolution equation for the transient NP factor $F_{NP}(p)$ given by
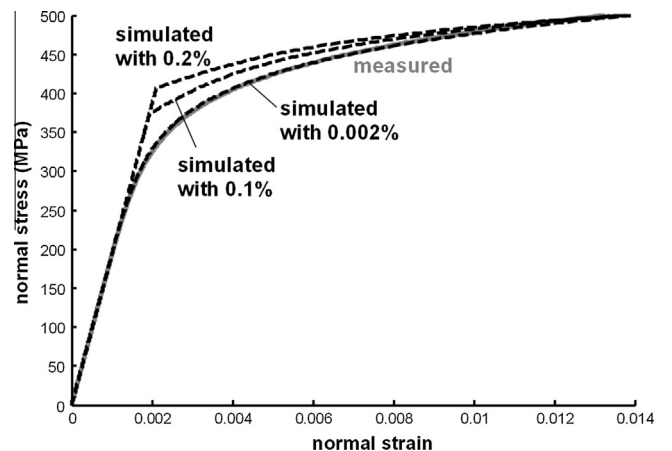

Fig. 4. Measured and simulated stress–strain curves adopting 0.2%, 0.1% or 0.002% plastic strain thresholds to define the yield surface (data for 316L stainless steel).

$$dF_{NP}(p) = [F_{NPt} - F_{NP}(p)] \cdot hr_{NP} \cdot dp,$$

$$F_{NPt} = \sqrt{\frac{2P_\sigma^2 n_\tau^2 + 2P_{\sigma\tau}^2 + 2P_\tau^2 n_\sigma^2 - 4P_{\sigma\tau}(P_\sigma + P_\tau)n_\sigma n_\tau}{P_\sigma^2 + 2P_{\sigma\tau}^2 + P_\tau^2}} \qquad (16)$$

where hr_{NP} is a NP hardening rate that dictates how fast the yield surface radius changes from its current value to its NP-hardened target value F_{NPt}.

In practice it is recommended to calibrate Tanaka's hardening rates hr_T and hr_{NP} satisfying the restriction $hr_T \leqslant hr_{NP} \leqslant 2.5 \cdot hr_T$, to avoid predicting a transient $F_{NP}(p)$ greater than 1.0, as verified from extensive simulations.

2.3. Strain-rate, temperature and creep effects on hardening

The presented hardening models assume quasi-static loading histories under temperatures much lower than the material melting point. However, strain-rate effects must be considered for very fast loadings, e.g. to model the hardness increase observed during an impact, or stress relaxation under long constant strain steps. Such viscoplastic strain-rate effects can be relevant in metallic structures. High temperature can activate as well creep mechanisms, resulting in an increase in inelastic deformation even under constant loads. For austenitic stainless steels such as 304L, such a deformation under constant loads may even happen at room temperature [25].

Creep and strain-rate effects are somewhat related, but for metals they can be conveniently separated by the order of magnitude of the associated strain rates [14]: viscoplastic creep mechanisms are usually associated with creep strain rates between 10^{-8}/s and 10^{-4}/s, while strain-rate effects become relevant for metals typically above 10^{-4}/s.

Several models have been proposed to incorporate strain-rate and temperature effects into the hardening behavior. One of the simplest is the popular Johnson–Cook's (J–C) model [26]. For a given uniaxial plastic strain rate $\dot{\varepsilon}_{x_{pl}} \equiv d\varepsilon_{x_{pl}}/dt$ applied under *monotonic* conditions at a fixed temperature Θ, J–C's model predicts a dynamically-corrected stress

$$\sigma_{xdyn} = \sigma_x \cdot \underbrace{\{1 + \alpha_{JC} \cdot \ln(|\dot{\varepsilon}_{x_{pl}}|/\dot{p}_0)\}}_{\text{strain-rate hardening factor}} \cdot \underbrace{\{1 - [(\Theta - \Theta_0)/(\Theta_f - \Theta_0)]^{m_{JC}}\}}_{\text{thermal softening factor}}$$

$$(17)$$

where σ_x is the associated stress under quasi-static conditions (calculated e.g. using Ramberg–Osgood's equation or any rate-independent incremental plasticity model) obtained at a reference temperature Θ_0 (usually set as room temperature), and $\alpha_{JC}, m_{JC}, \Theta_f$, and $\dot{p}_0$ are material constants: α_{JC} is the strain-rate hardening coefficient, m_{JC} is the thermal softening exponent, Θ_f is the melting temperature, and $\dot{p}_0$ is the quasi-static plastic strain rate below which dynamic effects are negligible, usually assumed $\dot{p}_0 = 2 \cdot 10^{-3}$/s for metals.

In this work, J–C's uniaxial model is assumed valid for multiaxial loadings, using the equivalent plastic strain rate $\dot{p} \equiv dp/dt$, where dp is the previously-defined equivalent plastic strain increment. Under uniaxial conditions, it follows that $dp = |d\varepsilon_{x_{pl}}|$, therefore $\dot{p} = |\dot{\varepsilon}_{x_{pl}}|$, allowing the definition of dynamic (rate-dependent) generalized plastic modulus coefficients $p_{dyn_i}(p)$

$$p_{dyn_i}(p) = p_i(p) \cdot \underbrace{\{1 + \alpha_{JC} \cdot \ln(\dot{p}/\dot{p}_0)\}}_{\text{strain-rate hardening factor}} \cdot \underbrace{\{1 - [(\Theta - \Theta_0)/(\Theta_f - \Theta_0)]^{m_{JC}}\}}_{\text{thermal softening factor}}$$

$$(18)$$

Therefore, strain-rate and temperature effects on strain hardening could be considered in incremental plasticity calculations by simply replacing the quasi-static $p_i(p)$ from Eq. (13) with the dynamic $p_{dyn_i}(p)$. For quasi-static loadings $(\dot{p} < \dot{p}_0)$, the above expression must be evaluated assuming $\dot{p} = \dot{p}_0$. It is important to emphasize that, for uniaxial loadings, this incremental formulation would exactly reproduce J–C's uniaxial model. However, its generalization to multiaxial loadings is just an approximation, and it should be verified with proper multiaxial tests under high strain rates, which is not the main focus of this work.

The incorporation of time-dependent creep in incremental plasticity models is a more challenging problem than the consideration of strain-rate effects [25]. One approach involves the so-called *unified viscoplasticity* (or unified hardening) approach, which assumes that all plastic and creep strains can be represented altogether in the same inelastic strain variable, being able to predict the coupled influence of creep strains on the strain-hardening behavior of the material. On the other hand, the *non-unified viscoplasticity approach* assumes a partition between plasticity and creep, i.e. plastic and creep strains are treated independently. These two approaches are beyond the scope of this work, but they are extensively discussed in [14].

3. State-space representation of the tension–torsion formulation

The set of differential equations presented in Eqs. (4)–(16) is usually stiff, i.e. some states can vary orders of magnitude faster than others, requiring very efficient numerical integration schemes with adjustable step increments to solve them. The numerical approach proposed in this work uses Gear's method for solving stiff systems of differential equations [27].

To apply Gear's method, a state-space representation of all presented incremental plasticity equations is adopted, including kinematic, isotropic, and NP hardening transient equations. In this representation, the stress and strain states, as well as all internal variables from the material, are represented in a single state vector $\vec{X}$, whose evolution is described by first-order differential equations. If M backstress components are chosen to represent the material behavior (with M typically greater than 4 for more refined calculations), then the state variable $\vec{X}$ from the proposed tension–torsion formulation becomes a (column) vector with $2M + 9$ elements, namely

$$\vec{X} = \begin{bmatrix} \vec{s}^T & \vec{e}^T & p & P_\sigma & P_\tau & P_{\sigma\tau} & F_{NP} & \vec{\beta}_1^T & \vec{\beta}_2^T & \dots & \vec{\beta}_M^T \end{bmatrix}^T \qquad (19)$$

where the 2×1 vectors $\vec{s}$ and $\vec{e} \equiv \vec{e}_{el} + \vec{e}_{pl}$ store the tension–torsion input/output stresses and strains, the scalar p is the current accumulated plastic strain, the next four elements store internal variables needed to predict the NP hardening evolution from Tanaka's model, and the last $2M$ elements store plastic memory from kinematic hardening through M two-dimensional backstress components.

For any given stress history, $\vec{s}$ is treated as a time input $\vec{s}(t)$ from which $\vec{e}(t)$ is calculated, and vice-versa for any given strain history. Note that the elastic and plastic strain components $\vec{e}_{el}$ and $\vec{e}_{pl}$ do not need to be individually stored in the state variable $\vec{X}$, because under tension–torsion they can be promptly computed at each simulation instant t from the relations $\varepsilon_{xel} = \sigma_x/E$, $\varepsilon_{xpl} = \varepsilon_x - \varepsilon_{xel}$, $\gamma_{xyel} = \tau_{xy}/G$, and $\gamma_{xypl} = \gamma_{xy} - \gamma_{xyel}$. Moreover, the assumed $y - z$ symmetry allows the calculation of the remaining strain and stress components from $\varepsilon_{yel} = \varepsilon_{zel} = -\nu\varepsilon_{xel}$ and $\varepsilon_{ypl} = \varepsilon_{zpl} = -0.5 \cdot \varepsilon_{xel}$, where under free-surface conditions $\sigma_y = \sigma_z = \tau_{xz} = \tau_{yz} = 0$ and $\gamma_{xz} = \gamma_{yz} = 0$. To solve the initial value problem using Gear's method [27], the state evolution must then be written in the form

$$d\vec{X}/dt = \vec{f}(\vec{X}, t) \qquad (20)$$

where t stands for time, and $\vec{f}(\vec{X}, t)$ is a non-linear vector function with $2M + 9$ elements as well.

For time-independent plasticity, this t parameter can be regarded not as an actual time, but instead just as an index used to account for the load history sequence assuming a data sampling rate with a constant unit frequency, supposing it uses e.g. a fixed 1 s interval between samples. So, if $\vec{e}(503)$ and $\vec{e}(504)$ are measured strains from two consecutive data samples number 503 and 504, then the rate $d\vec{e}(t)/dt$ can be linearly estimated for all "instants" $503\,s \leqslant t < 504\,s$ from the difference $[\vec{e}(504) - \vec{e}(503)]$. However, if time-dependent models had been included in the simulation to account e.g. for creep, strain-rate, or other viscous effects, then this parameter t would need to correspond to the actual time from each measured state.

At each integration step, the current backstress is calculated through $\vec{\beta} \equiv \vec{\beta}_1 + \vec{\beta}_2 + \ldots + \vec{\beta}_M$, to obtain the normal vector $\vec{n} = (\vec{s} - \vec{\beta})/S \equiv [n_\sigma \quad n_\tau]^T$. If the norm of $\vec{n}$ is equal to 1.0 (within some very small numerical tolerance, e.g. 10^{-10}) and the stress state is trying to move outside of the yield surface (i.e. $d\vec{s}^T \cdot \vec{n} > 0$ under stress control or $d\vec{e}^T \cdot \vec{n} > 0$ under strain control), then plastic straining is currently under way. In this case, the current plastic straining direction $\vec{n} \equiv [n_\sigma \quad n_\tau]^T$ can be used to calculate the generalized plastic modulus coefficients $p_i(p)$ from Eq. (13), to then obtain the current generalized plastic modulus $P = (2/3) \cdot \sum_{i=1}^{M} p_i(p) \cdot \left(\Delta r_i - \chi_i^* \cdot m_i^* \cdot \gamma_i \cdot \vec{\beta}_i^T \cdot \vec{n} \right)$, in addition to the current target value F_{NPt} of the NP factor using Eq. (16), resulting in the state-space equation

state $\vec{X}$ along the t parameter, given the initial condition $\vec{X}(0)$, which should be null for a virgin specimen.

4. Experimental results

To verify the prediction capabilities of the presented numerical framework, tension–torsion experiments have been performed on annealed tubular 316L stainless steel specimens in a servo-hydraulic multiaxial testing machine, shown in Fig. 5. A thin wall of 1.5 mm is usually adopted in tubular specimens, to avoid having to deal with stress gradient effects across the thickness. But, since some experiments in this work involve large compression strains, the minimum wall thickness is increased from 1.5 to 2.0 mm to avoid buckling. On the critical section, the tubular specimen has external and internal diameters $d_{ext} = 16$ mm and $d_{int} = 12$ mm. Engineering stresses and strains are calculated from load and torque measurements made by the machine load cells and from an axial/torsional extensometer, and then converted to true stresses and strains. The engineering shear stresses include the elastoplastic gradient correction recommended by ASTM E2207-08 [28].

The cyclic properties of this 316L steel are obtained from uniaxial tests, resulting in fitted Ramberg–Osgood uniaxial cyclic hardening coefficient $H_c = 74$ MPa and exponent $h_c = .123$, with Young's modulus $E = 193$ GPa, Poisson ratio $v = 0.3$, and $G = E/(2 + 2v) \cong 74$ GPa. To improve the calculation accuracy, the

$$
d\vec{X} = \begin{bmatrix} d\vec{s} \\ d\vec{e} \\ dp \\ dP_\sigma \\ dP_\tau \\ dP_{\sigma\tau} \\ dF_{NP} \\ d\vec{\beta}_1 \\ d\vec{\beta}_2 \\ \vdots \\ d\vec{\beta}_M \end{bmatrix} = \begin{bmatrix} d\vec{s}(t) \text{ or } 2G \cdot d\vec{e} - 2G \cdot [d\vec{e}^T \cdot \vec{n} \cdot 2G/(2G + P)] \cdot \vec{n} \\ d\vec{s}/(2G) + (d\vec{s}^T \cdot \vec{n}) \cdot \vec{n}/P \text{ or } d\vec{e}(t) \\ (2/3) \cdot (d\vec{s}^T \cdot \vec{n})/P \\ (n_\sigma^2 - P_\sigma) \cdot hr_T \cdot dp \\ (n_\tau^2 - P_\tau) \cdot hr_T \cdot dp \\ (n_\sigma n_\tau - P_{\sigma\tau}) \cdot hr_T \cdot dp \\ (F_{NPt} - F_{NP}) \cdot hr_{NP} \cdot dp \\ p_1 \cdot \left\{ \vec{n} \cdot \Delta r_1 - \chi_1^* \cdot m_1^* \cdot \gamma_1 \cdot [\delta_1 \cdot \vec{\beta}_1 + (1 - \delta_1) \cdot \left(\vec{\beta}_1^T \cdot \vec{n} \right) \cdot \vec{n}] \right\} \cdot dp \\ p_2 \cdot \left\{ \vec{n} \cdot \Delta r_2 - \chi_2^* \cdot m_2^* \cdot \gamma_2 \cdot [\delta_2 \cdot \vec{\beta}_2 + (1 - \delta_2) \cdot \left(\vec{\beta}_2^T \cdot \vec{n} \right) \cdot \vec{n}] \right\} \cdot dp \\ \vdots \\ p_M \cdot \left\{ \vec{n} \cdot \Delta r_M - \chi_M^* \cdot m_M^* \cdot \gamma_M \cdot [\delta_M \cdot \vec{\beta}_M + (1 - \delta_M) \cdot \left(\vec{\beta}_M^T \cdot \vec{n} \right) \cdot \vec{n}] \right\} \cdot dp \end{bmatrix} \tag{21}
$$

For a known stress history, the given rates $d\vec{s}(t)/dt$ are used in the first row of Eq. (21), while the corresponding $d\vec{e}(t)/dt$ are obtained as shown in the second row on the left, calculated from Eq. (4) and Hooke's law. If the tension–torsion loading is instead under strain control, then the given rates $d\vec{e}(t)/dt$ are used in the second row of Eq. (21), while the corresponding $d\vec{s}(t)/dt$ are obtained as shown in the first row on the right, calculated from the inverse stress–strain problem.

On the other hand, if the current norm of $\vec{n}$ is smaller than 1.0 (within some very small numerical tolerance), or if the stress state is trying to move inside the yield surface (i.e. in an elastic unloading state with $d\vec{s}^T \cdot \vec{n} < 0$ or even $d\vec{e}^T \cdot \vec{n} < 0$), then the stress/strain increment is purely elastic, and all $\vec{f}(\vec{X}, t)$ terms from Eq. (21) become zero since in this case $P \to \infty$ and $dp = 0$, except for the first two rows, which become Hooke's law $d\vec{s} = 2G \cdot d\vec{e}$ and $d\vec{e} = d\vec{s}/(2G)$, respectively. Once Eq. (20) has been defined for both elastic and elastoplastic conditions, it can be numerically integrated using Gear's method [27] to calculate the evolution of the

backstress is divided into $M = 5$ additive components, following Chaboche's idea [17]. Jiang–Sehitoglu's kinematic hardening model [19] is adopted, using its $\gamma_i = \delta_i = 1$, $m_i = 0$, and the parameter calibration procedure described in [20]: for a chosen set of generalized plastic modulus coefficients $p_i = \{6176, 786, 100, 12.7, 1.62\}$ MPa, the resulting saturation values for the backstress components become $\Delta r_i \cong \{66, 85, 109, 141, 217\}$ MPa. No significant strain-rate or creep effects were identified in the experiments, therefore they were not included in the adopted formulation.

Uniaxial ratcheting experiments are used to calibrate the adjustable exponents X_i needed in Jiang–Sehitoglu's model, using an RMS fit with respect to the corresponding simulations. Such a calibration is a computationally-intensive and exhaustive ad hoc task, requiring each uniaxial ratcheting experiment to be simulated several times until the measured and simulated hysteresis loops coincide within some tolerable RMS error. The presented 2D formulation is particularly most valuable in this calibration procedure, since it allows each simulation to be performed much faster than using a 6D approach.
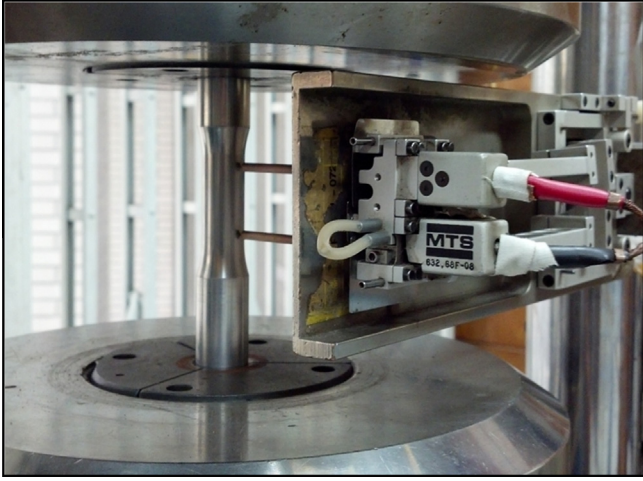
Fig. 5. Tension–torsion testing machine and extensometer mounted on a tubular specimen.

The adopted calibration procedure initially sets all ratcheting exponents X_i as equal to 1.0, which would reproduce Chaboche's original NLK model. For the adopted $M = 5$, this results in an initial guess $X_i = \{1,1,1,1,1\}$ for the M ratcheting calibration parameters. The uniaxial ratcheting experiments involve tension–compression loadings on the tubular specimens with significant mean component. It has been observed that the first exponent X_1 controls the ratcheting behavior for lower stress ranges $\Delta\sigma_x$, in which case the outer hardening surfaces are barely activated. Therefore, it is calibrated first, for uniaxial ratcheting histories with such low values of $\Delta\sigma_x$. If the simulation overpredicts the ratcheting effect with respect to the measurements, then the value of X_1 is increased by some chosen calculation percentage, e.g. 10%, otherwise it is decreased, until the RMS error between the simulation and measured hysteresis loops is reduced to an acceptable threshold. Notice that Chaboche's $X_i = 1$ usually overpredicts ratcheting effects, while $X_i \to \infty$ predicts no ratcheting, so usual calibrated exponents are such that $1 \leqslant X_i < \infty$.

Once X_1 is calibrated, uniaxial ratcheting tests with increased $\Delta\sigma_x$ are then used to iteratively calibrate X_2, and so on, until X_5 is calibrated from tests with large $\Delta\sigma_x$. The chosen $\Delta\sigma_x$ level for each calibration step must be larger than the diameter of the hardening surface associated with each X_i, to guarantee this surface has been significantly activated. For the studied 316L stainless steel, the calibrated exponents resulted in $X_i = \{1,1,2.9,3,4\}$, which were able to calibrate the uniaxial ratcheting experiments within an RMS error in the resulting strains of less than $0.0012 = 0.12\%$, as
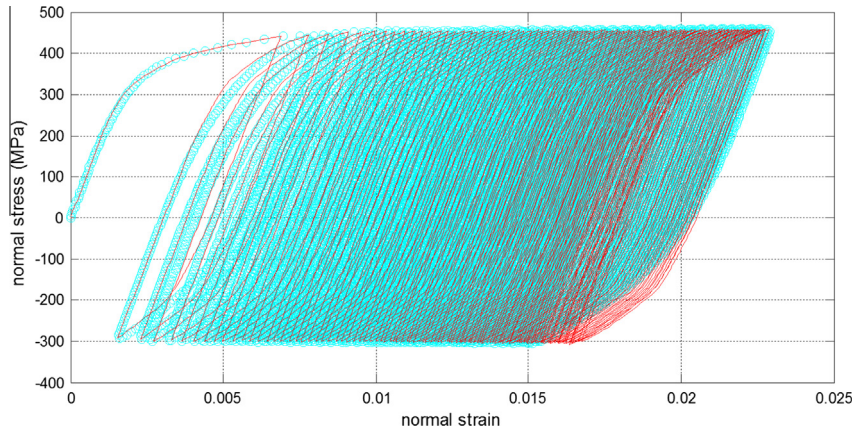
seen in Fig. 6 for loops with σ_{max} = 450 MPa and σ_{min} = −300 MPa, thus with $\Delta\sigma_x$ = 750 MPa.

After calibrating the incremental plasticity model, strain-controlled tension–torsion load cycles were applied to (different) tubular specimens, for non-proportional 90° out-of-phase circular strain paths, see Fig. 7(left). These circular paths are particularly challenging because they involve high NP hardening effects and transients, as well as several *neutral loading* steps where the stress path follows the perimeter of the yield surface (thus $d\vec{s}^T \cdot \vec{n} = 0$), which is a known configuration for numerical instability. An additional hardening coefficient $\alpha_{NP} = 0.86$ is then iteratively calibrated from the measured circular paths to minimize the RMS errors between simulated and measured strain paths. NP hardening rates are also calibrated in the same way, resulting in $hr_{NP} = 1.3$ for an assumed $hr_T = hr_{NP}/2$, giving $hr_T = 0.65$.

From the calibrated values, and approximating $2G \cong 148{,}000$ MPa, the state-space equation for this annealed 316L steel under a strain-controlled condition with given infinitesimal $d\vec{e}(t)$ increments becomes, for a general elastoplastic step,

$$d\vec{X} = \begin{bmatrix} d\vec{s} \\ d\vec{e} \\ dp \\ dP_\sigma \\ dP_\tau \\ dP_{\sigma\tau} \\ dF_{NP} \\ d\vec{\beta}_1 \\ d\vec{\beta}_2 \\ d\vec{\beta}_3 \\ d\vec{\beta}_4 \\ d\vec{\beta}_5 \end{bmatrix} = \begin{bmatrix} 148{,}000 \cdot d\vec{e} - 148{,}000 \cdot [d\vec{e}^T \cdot \vec{n} \cdot 148{,}000/ \\ \qquad (148{,}000 + P)] \cdot \vec{n} \\ d\vec{e}(t) \\ (2/3) \cdot (d\vec{s}^T \cdot \vec{n})/P \\ (n_\sigma^2 - P_\sigma) \cdot 0.65 \cdot dp \\ (n_\tau^2 - P_\tau) \cdot 0.65 \cdot dp \\ (n_\sigma n_\tau - P_{\sigma\tau}) \cdot 0.65 \cdot dp \\ (F_{NPt} - F_{NP}) \cdot 1.3 \cdot dp \\ 6176 \cdot \{\vec{n} \cdot 66 - (|\vec{\beta}_1|/66)^1 \cdot \vec{\beta}_1\} \cdot dp \\ 786 \cdot \{\vec{n} \cdot 85 - (|\vec{\beta}_2|/85)^1 \cdot \vec{\beta}_2\} \cdot dp \\ 100 \cdot \{\vec{n} \cdot 109 - (|\vec{\beta}_3|/109)^{2.9} \cdot \vec{\beta}_3\} \cdot dp \\ 12.7 \cdot \{\vec{n} \cdot 141 - (|\vec{\beta}_4|/141)^3 \cdot \vec{\beta}_4\} \cdot dp \\ 1.62 \cdot \{\vec{n} \cdot 217 - (|\vec{\beta}_5|/217)^4 \cdot \vec{\beta}_5\} \cdot dp \end{bmatrix} \quad (22)$$

where $\vec{\beta} \equiv \vec{\beta}_1 + \vec{\beta}_2 + \cdots + \vec{\beta}_M, \vec{n} = (\vec{s} - \vec{\beta})/S \equiv [\,n_\sigma \quad n_\tau\,]^T$, and

$$P = \frac{2}{3} \cdot \left\{ 6176 \cdot \left[66 - \frac{|\vec{\beta}_1|}{66} \cdot \vec{\beta}_1^T \cdot \vec{n} \right] + 786 \cdot \left[85 - \frac{|\vec{\beta}_2|}{85} \cdot \vec{\beta}_2^T \cdot \vec{n} \right] \right.$$
$$+ 100 \cdot \left[109 - \left(\frac{|\vec{\beta}_3|}{109}\right)^{2.9} \cdot \vec{\beta}_3^T \cdot \vec{n} \right] + + 12.7 \cdot \left[141 - \left(\frac{|\vec{\beta}_4|}{141}\right)^3 \cdot \vec{\beta}_4^T \cdot \vec{n} \right]$$
$$\left. + 1.62 \cdot \left[217 - \left(\frac{|\vec{\beta}_5|}{217}\right)^4 \cdot \vec{\beta}_5^T \cdot \vec{n} \right] \right\} \cdot [1 + 0.86 \cdot F_{NP}]^{\frac{1}{0.123}} \cdot dp \quad (23)$$

Fig. 6. Measured (light markers) and fitted (dark lines) $\sigma_x \times \varepsilon_x$ hysteresis loops from stress-controlled uniaxial ratcheting experiments with stresses between −300 and 450 MPa.
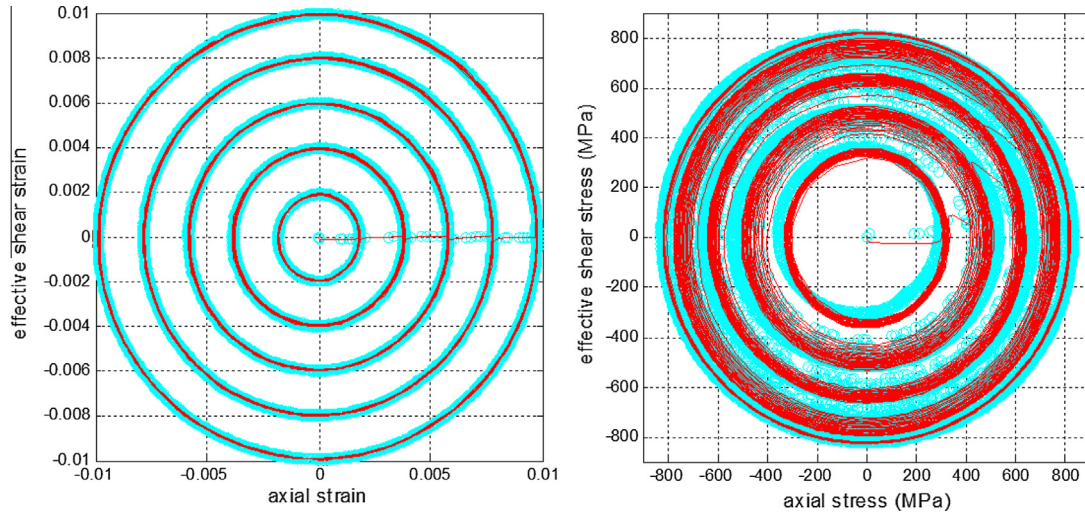
Fig. 7. Left: circular $\varepsilon_x \times \gamma_{xy}/\sqrt{3}$ strain paths applied to the tension–torsion tubular specimens with amplitudes 0.2%, 0.4%, 0.6%, 0.8% and 1.0%; Right: resulting $\sigma_x \times \tau_{xy}\sqrt{3}$ stress paths experimentally measured (light lines) and predicted using the simulator (dark lines).
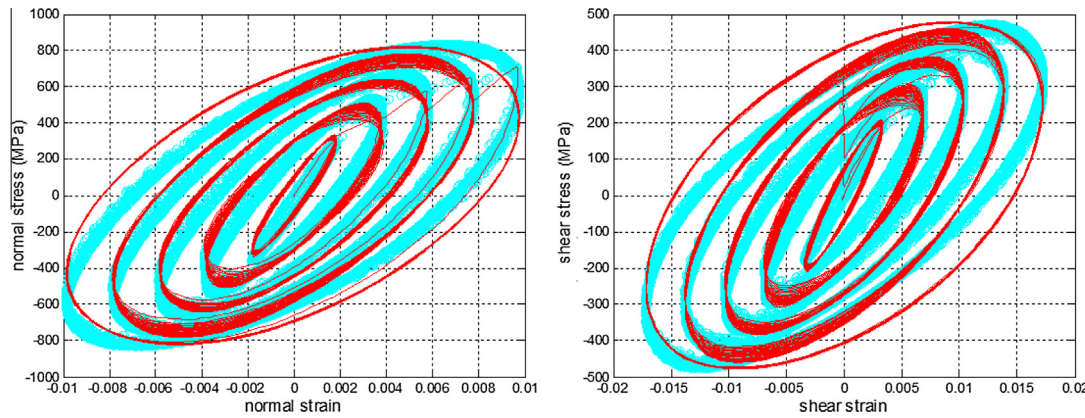

Fig. 8. Normal and shear hysteresis loops from applied circular tension–torsion strain histories, either experimentally measured (light lines) or predicted using the simulator (dark lines).
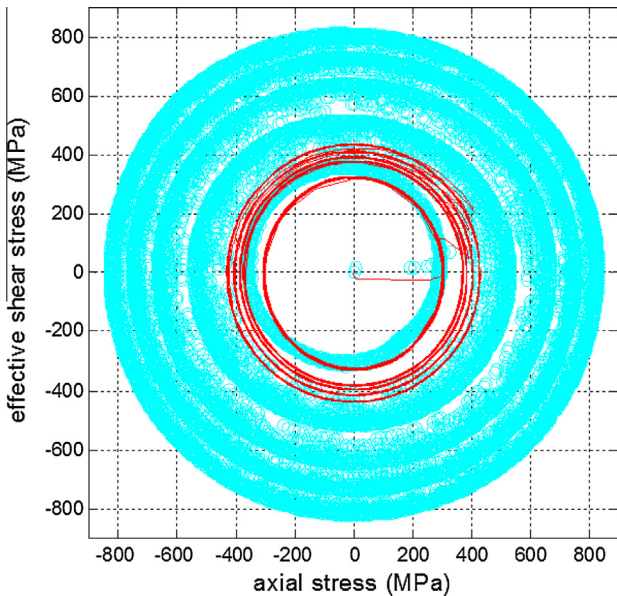

Fig. 9. Resulting $\sigma_x \times \tau_{xy}\sqrt{3}$ stress paths wrongfully predicted using the simulator neglecting NP hardening effects (dark lines), and the actual experimentally measured paths (light lines).

assuming generalized plastic modulus coefficients $p_i(p)$ that only consider the NP transient, while for simplicity ignoring the isotropic hardening transient (i.e. setting $hr_c \rightarrow \infty$), thus

$$p_i(p) = p_i(0) \cdot [1 + 0.86 \cdot F_{NP}]^{1/0.123} \qquad (24)$$

When Eq. (22) is simulated using Gear's method [27] with a very refined relative precision 10^{-6} and absolute precision 10^{-9}, the applied circular tension–torsion strain paths result in the stress paths from Fig. 7(right), showing a very reasonable agreement with experimental results. Fig. 8 plots the corresponding normal and shear hysteresis loops. Note that both kinematic and NP hardening transients are captured by the implemented incremental plasticity simulation, and that the NP hardening effect cannot be neglected, as shown in Fig. 9.

The presented simulation from Figs. 7 and 8 involves 94,473 input strain points, taking in the proposed numerical framework 1509 s (about 25 min) to be computed in an i7-3770 CPU at 3.4 GHz with 16 GB RAM memory. To evaluate the numeric efficiency of the proposed 2D approach, an identical incremental plasticity simulation (for the same 94,473 points) is performed, but using a 6D (instead of 2D) stress–strain formulation. Even if the same efficient Gear's method is used to solve the equations, the 6D simulation takes 8650 s (over 144 min) to be computed in the same CPU, i.e. about 5.7 times longer.
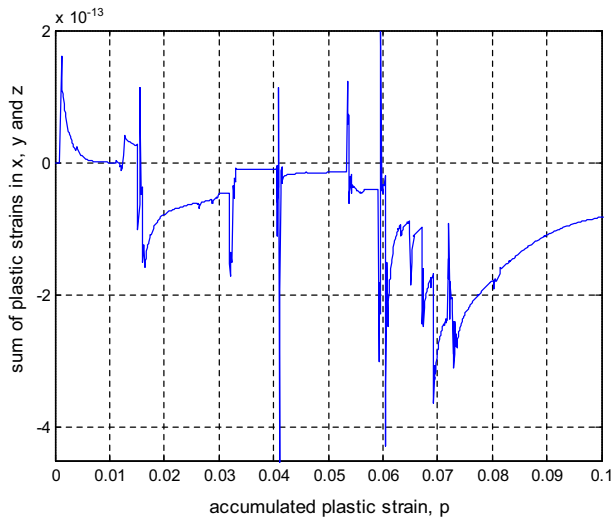
Fig. 10. Residual error in the $\varepsilon_{xpl} + \varepsilon_{ypl} + \varepsilon_{zpl}$ summation for the 6D incremental plasticity formulation, whose stability to avoid violating plastic strain incompressibility adds computational cost.

The traditional 6D incremental plasticity formulation is slower due to its higher dimension, since for the adopted $M = 5$ backstress components it would imply in a state variable $\vec{X}$ with $6M + 29 = 59$ instead of $2M + 9 = 19$ elements (i.e. it would require the solution of a set of 59 instead of 19 stiff differential equations). Moreover, the 6D formulation does not guarantee plastic strain incompressibility, therefore numerical errors could wrongfully result in a sum of plastic strains $\varepsilon_{xpl} + \varepsilon_{ypl} + \varepsilon_{zpl}$ different than zero. Gear's method is able to keep this summation error below the chosen absolute precision 10^{-9}, see Fig. 10, but at a high computational cost. The proposed 2D formulation, on the other hand, automatically and *exactly* satisfies plastic strain incompressibility because it adopts $\varepsilon_{ypl} = \varepsilon_{zpl} = -0.5\varepsilon_{xel}$ and thus $\varepsilon_{xpl} + \varepsilon_{ypl} + \varepsilon_{zpl} = 0$, saving considerable computational time.

5. Conclusions

In this work, a computationally-efficient 2D tension–torsion incremental plasticity formulation was introduced, integrating non-linear kinematic (NLK), isotropic, and NP hardening effects, with the possible introduction of strain-rate and temperature effects as well. The proposed approach is able to exactly reproduce most modern NLK models, such as Chaboche's, Jiang–Sehitoglu's, Ohno-Wang II, and Delobelle's, among several others. Besides reducing the state dimension and the number of required differential equations by a factor of at least 3, the 2D formulation also automatically and exactly satisfies the plastic strain incompressibility condition, resulting in a reduction of the computational cost and time by a factor of at least 5. Non-proportional tension–torsion experiments with 316L steel tubular specimens validated the proposed approach.

Acknowledgments

References

[1] Buczynski A, Glinka G. Multiaxial stress–strain notch analysis, multiaxial fatigue and deformation: testing and predictions. ASTM STP 1378; 2000. p. 82–98.
[2] Buczynski A, Glinka G. An analysis of elasto-plastic strains and stresses in notched bodies subjected to cyclic non-proportional loading paths. In: Biaxial/multiaxial fatigue and fracture. Elsevier; 2003. p. 265–83.
[3] McDonald RJ, Socie DF. A technique to estimate the local multiaxial elastic–plastic behavior from a purely elastic solution. Eng Fract Mech 2011;78:1696–704.
[4] Köettgen VB, Barkey ME, Socie DF. Pseudo stress and pseudo strain based approaches to multiaxial notch analysis. Fatigue Fract Eng Mater Struct 1995;18:981–1006.
[5] Köettgen VB, Barkey ME, Socie DF. Pseudo stress and pseudo strain based approaches to multiaxial notch analysis. Fracture control program report #169. U Illinois at Urbana-Champaign; 1995.
[6] Bannantine JA, Socie DF. A variable amplitude multiaxial fatigue life prediction method. Fatigue under biaxial and multiaxial loading, vol. 10. ESIS publ.; 1991. p. 35–51.
[7] Socie DF, Marquis GB. Multiaxial fatigue. Warrendale, PA: Society of Automotive Engineers, Inc.; 2000.
[8] Meggiolaro MA, Castro JTP. Prediction of non-proportionality factors of multiaxial histories using the moment of inertia method. Int J Fatigue 2014;61:151–9.
[9] Meggiolaro MA, Castro JTP, Wu H. A general class of non-linear kinematic models to predict mean stress relaxation and multiaxial ratcheting in fatigue problems – part I: Ilyushin spaces. Int J Fatigue 2015;82:158–66.
[10] Mróz Z. On the description of anisotropic workhardening. J Mech Phys Solids 1967;15(3):163–75.
[11] Garud YS. A new approach to the evaluation of fatigue under multiaxial loading. Trans ASME J Eng Mater Technol 1981;103:118–25.
[12] Krieg RD. A practical two-surface plasticity theory. J Appl Mech 1975;42(3):641–6.
[13] Dafalias YF, Popov EP. Plastic internal variables formalism of cyclic plasticity. J Appl Mech 1976;43(4):645–51.
[14] Chaboche JL. A review of some plasticity and viscoplasticity constitutive theories. Int J Plast 2008;24(10):1642–93.
[15] Jiang Y, Sehitoglu H. Comments on the Mróz multiple surface type plasticity models. Int J Solids Struct 1996;33(7):1053–68.
[16] Armstrong PJ, Frederick CO. A mathematical representation of the multiaxial Bauschinger effect. CEGB report RD/B/N731. Berkeley Nuclear Laboratory; 1966.
[17] Chaboche JL, Dang Van K, Cordier G. Modelization of the strain memory effect on the cyclic hardening of 316 stainless steel. In: Transactions of the fifth international conference on structural mechanics in reactor technology. Div. L, Berlin; 1979.
[18] Meggiolaro MA, Castro JTP, Wu H. A general class of non-linear kinematic models to predict mean stress relaxation and multiaxial ratcheting in fatigue problems – part II: generalized yield surface translation rule. Int J Fatigue 2015;82:167–78.
[19] Jiang Y, Sehitoglu H. Modeling of cyclic ratchetting plasticity, part I: development of constitutive relations. ASME J Appl Mech 1996;63(3):720–5.
[20] Jiang Y, Sehitoglu H. Modeling of cyclic ratchetting plasticity, part II: comparison of model simulations with experiments. ASME J Appl Mech 1996;63(3):726–33.
[21] Ohno N, Wang JD. Kinematic hardening rules with critical state of dynamic recovery, part I: formulations and basic features for ratchetting behavior. Int J Plast 1993;9:375–90.
[22] Delobelle P, Robinet P, Bocher L. Experimental study and phenomenological modelization of ratchet under uniaxial and biaxial loading on an austenitic stainless steel. Int J Plast 1995;11:295–330.
[23] Burlet H, Cailletaud G. Numerical techniques for cyclic plasticity at variable temperature. Eng Comput 1986;3:143–53.
[24] Tanaka E. A nonproportionality parameter and a cyclic viscoplastic constitutive model taking into account amplitude dependences and memory effects of isotropic hardening. Eur J Mech – A/Solids 1994;13:155–73.
[25] Taleb L, Cailletaud G. Cyclic accumulation of the inelastic strain in the 304L SS under stress control at room temperature: ratcheting or creep? Int J Plast 2011;27:1936–58.
[26] Johnson GR, Cook WH. A constitutive model and data for metals subjected to large strains, high strain rates and high temperatures. In: Proceeding of the 7th international symposium on ballistics; 1983. p. 541–7.
[27] Gear CW. The automatic integration of stiff ordinary differential equations (with discussion). Information processing. North-Holland; 1969 [68(1), p. 187–93].
[28] ASTM E2207-08. Standard practice for strain-controlled axial–torsional fatigue testing with thin-walled tubular specimens; 2013.